Acoustically Accelerated Neural Differentiation of Human Embryonic Stem Cells

Chao Sun[1,2#], Yinhua Dong[3#], Jun Wei[4], Meng Cai[4], Dongfang Liang[5], Yongqing Fu[6], You Zhou[7], Yi Sui[8], Fangda Wu[2], Roman Mikhaylov[2], Hanlin Wang[2], Feifei Fan[9], Zhihua Xie[10], Mercedes Stringer[2], Zhiyong Yang[11], Zhenlin Wu[12], Liangfei Tian[13], Xin Yang[2]*

[1] School of Life Sciences, Northwestern Polytechnical University, Xi'an, 710072, P.R. China
[2] Department of Electrical and Electronic Engineering, School of Engineering, Cardiff University, Cardiff, CF24 3AA, United Kingdom
[3] Department of Neurology, Tianjin 4th Centre Hospital Affiliated to Nankai University, Tianjin, 300140, P.R. China
[4] iRegene Therapeutics Co., Ltd, Wuhan, 430070, P.R. China
[5] Department of Engineering, University of Cambridge, Cambridge, CB2 1PZ, United Kingdom
[6] Faculty of Engineering and Environment, Northumbria University, Newcastle Upon Tyne, Newcastle, NE1 8ST, United Kingdom
[7] Systems Immunity University Research Institute and Division of Infection and Immunity, School of Medicine, Cardiff University, Cardiff, CF14 4XN, United Kingdom
[8] School of Engineering and Materials Science, Queen Mary University of London, London, E1 4NS, United Kingdom
[9] Emergency Department, Xijing Hospital, Xi'an, 710032, P.R. China
[10] Department of Civil Engineering, School of Engineering, Cardiff University, Cardiff, CF24 3AA, United Kingdom
[11] School of Mechanical Engineering, Tianjin University, Tianjin, 300072, PR China
[12] School of Optoelectronic Engineering and Instrumentation Science, Dalian University of Technology, Dalian, 116023, PR China
[13] MOE Key Laboratory of Biomedical Engineering, Department of Biomedical Engineering, Zhejiang University, Hangzhou, 310027, China

[#]Authors contributed equally to this work.
*Corresponding authors:
Dr. Xin Yang (e-mail: YangX26@cardiff.ac.uk)

Abstract

Human embryonic stem cells (hESCs) and their derived products offer great promise for targeted therapies and drug screening, however, the hESC differentiation process of mature neurons is a lengthy process. To accelerate the neuron production, an acoustic stimulator producing surface acoustic waves (SAWs) is proposed and realized by clamping a flexible printed circuit board (PCB) directly onto a piezoelectric substrate. Neural differentiation of the hESCs is greatly accelerated after application of the acoustic stimulations. Acceleration mechanisms for neural differentiation have been explored by bulk RNA sequencing, quantitative polymerase chain reaction (qPCR) and immunostaining. The RNA sequencing results show changes of extracellular matrix-related and physiological activity-related gene expression in the low or medium SAW dose group and the high SAW dose group, respectively. The neural progenitor cell markers, including *Pax6*, *Sox1*, *Sox2*, *Sox10* and *Nkx2-1*, are less expressed in the SAW dose groups compared with the control group by the qPCR. Other genes including *Alk*, *Cenpf*, *Pcdh17*, and *Actn3* are also found to be regulated by the acoustic stimulation. Moreover, the immunostaining confirmed that more mature neuron marker *Tuj1*-positive cells, while less stem cell marker *Sox2*-positive cells, are presented in the SAW dose groups. These results indicate that the SAW stimulation accelerated neural differentiation process. The acoustic stimulator fabricated by using the PCB is a promising tool in regulation of stem cell differentiation process applied in cell therapy.

Keywords

Embryonic stem cell, surface acoustic wave, acoustofluidics, interdigital transducer, neural differentiation

1. INTRODUCTION

The human embryonic stem cells (hESCs) offer reliable and abundant sources for studies of cellular biology, tissue engineering, treatment of neurodegenerative diseases, and pharmacological screens [1]. Neural stem cells (NSCs) derived from these hESCs are the sources of neurons, oligodendrocytes, and astrocytes [2]. Transplantation of NSCs is a promising treatment for neurological diseases, regeneration of neural cells and restoration of microenvironment at the injury site [3]. Currently neural differentiation process is mainly achieved by biological stimulations which require a long and complicated process up to weeks or months. This severely hinders the high yields of usable neuron populations for therapeutics.

Apart from those biological toolkits, various types of physical stimuli (such as those based on optics [4], electronics [5, 6], magnetics [7], microelectromechanical systems (MEMS) [8], topographical materials [9] and microfluidics [10]) have been explored as strategies to regulate *in vitro* neural differentiation of embryonic stem cells. For example, low intensity pulsed ultrasound (LIPUS) has been proven to promote neural lineages derived from various stem cells, and regulate cellular proliferation, differentiation, and membrane channels [11-13].

Surface acoustic waves (SAWs), with frequencies from a few MHz to a few GHz, can produce nanoscale vibrations with their wavelengths comparable to or much smaller than cells [14]. SAWs have advantages of easy integration with other systems such as microfluidics, as its configurations and materials are almost independent from other integrated systems [15]. These features allow SAW transducers to be developed as versatile tools for manipulating and characterizing cells [16], bacteria [17], model organism [18, 19], and extracellular vesicles [20]. Significantly increased cell migration [21, 22] and proliferation abilities [23], and enhanced cell metabolism and stiffness as the result of direct mechanical stimulation induced by SAWs have been demonstrated [24]. SAW-mediated intracellular delivery of siRNA into adherent [25] and non-adherent cells [26] were also demonstrated, which leads to the application for introducing the small molecules into the stem cells.

The underlying mechanisms for such effectively mechanical stimulations are the biophysical events of protein chains that are linked extracellular matrix (ECM) with plasma membranes, actin cytoskeleton [27], translation of relevant proteins, and their transcription and DNA sequences [28]. When the SAWs interact with the fluid, the acoustic energy is diffracted into the fluid in a form of leaky SAWs producing a distribution of acoustic pressure, which induces medium streaming and micro-circulation, and exerts a radiation force to the cells. SAWs also cause direct mechanical vibration applied to the cells which are directly attached to the vibrational substrate [29]. Such high-frequency external pressure/forces are fully controllable to produce precise stimulation parameters, which is unique for the fine-tuning of mechano-transduction proteins during the neural differentiation process of the hESCs.

SAW devices are generally manufactured through photolithography process by patterning interdigital transducers (IDTs) on a piezoelectric substrate such as lithium niobate ($LiNbO_3$). To minimize the strong dependence of cleanroom facilities for preparing SAW devices, our group explored an alternative and effective technique [30], in which a rigid printed circuit board (PCB) pre-patterned with a metal interdigital electrode (IDE) was mechanically clamped onto a $LiNbO_3$ wafer to produce SAWs. We further proposed to apply flexible laminates as thin film flexible PCBs (FPCBs), which possess advantages of superior mechanical properties, high flexibility, light weight and good thermal stability [31]. Using these FPCBs pre-patterned with IDEs offer benefits in reduction of device production time and avoiding the requirement of cleanroom facilities. Fast prototyping and testing using these alternative acoustofluidic devices

become readily feasible owing to great flexibility and increased package density of the FPCB [32].

Given the promise of using the hESCs derived neural lineage cells in treatment of neural degenerative diseases together with long-standing challenges associated with the neural differentiation, we proposed to accelerate these processes by using a FPCB SAW-based cell stimulation (FSCS) device. The device can be conveniently deployed in the batch simulation of hESC owing to its ability to on-demand fabrication. Our data demonstrated that SAW stimulation accelerated neural differentiation process. The SAW accelerated production of neural lineage cells has great potentials for drug screening and cell-based therapies.

2. MATERIALS AND METHODS

2.1. Device design and principle of SAW stimulation

The SAW device used for stimulation is prepared using a fast-prototyping technique as shown in Figure 1a. Radio frequency (RF) signals are applied to a $LiNbO_3$ substrate via IDEs of the FPCB, which produces SAWs propagating towards a polydimethylsiloxane (PDMS)-made cell chamber bonded onto the $LiNbO_3$ substrate. The FSCS is driven by the amplified RF signals as the system setup shown in Figure 1b. The SAWs contact the medium inside the PDMS chamber and form leaky SAWs. This causes part of the SAWs to be refracted into the liquid medium as a longitudinal wave [33]. Both the leaky SAWs and surface vibrations of the $LiNbO_3$ substrate interact with the biological cells attached to the surface of the $LiNbO_3$ substrate. The inset of Figure 1a displays the analytic model of the FSCS device, in which an edge wave from the PDMS-$LiNbO_3$-fluid contact point and a plane wave emanated from the vibration of the $LiNbO_3$ substrate to the fluid are combined to propagate in the medium.

(a)

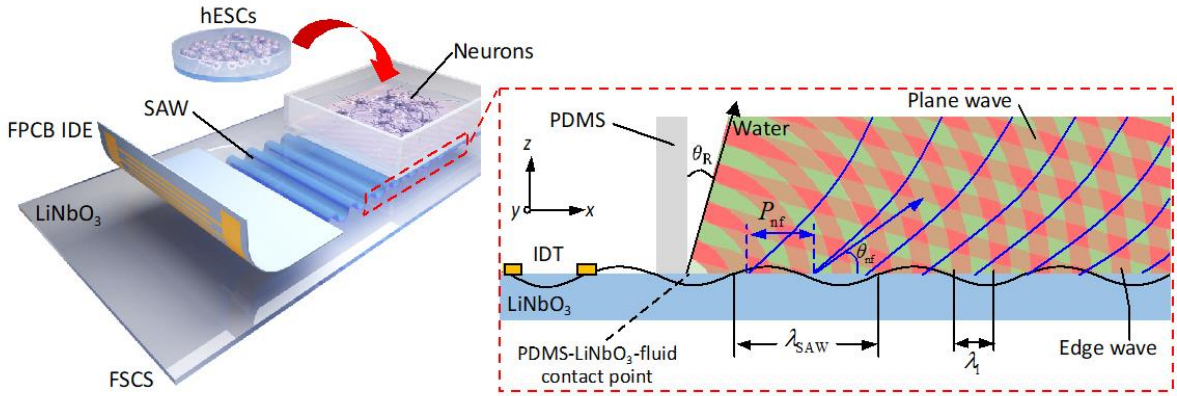

(b)

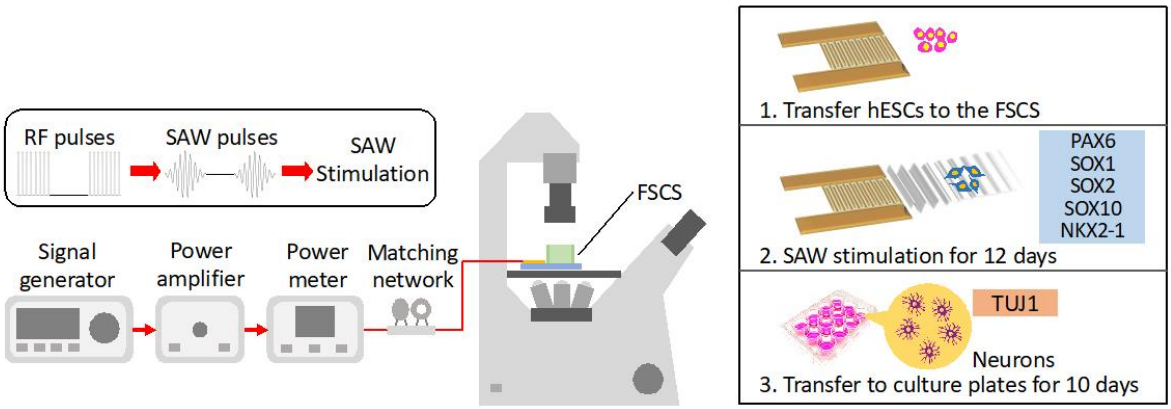

Figure 1. The flexible printed circuit board (FPCB) surface acoustic wave (SAW)-based cell stimulation (FSCS) device used for cell stimulation. (a) The 3D model of the FSCS, consisting of a SAW generator and a cell chamber. Human embryonic stem cells (hESCs) are seeded in the FSCS. The SAW generator is made by coupling FPCB interdigital electrodes (IDEs) to a $LiNbO_3$ substrate. The inset shows the cross-sectional view of the analytic model of the FSCS device. An interdigital transducer (IDT) generates SAW propagating towards the cell chamber. The plane and edge waves create static interference pressure patterns in the fluid, resulting in a near-field pattern of acoustic pressure with the period of P_{nf} and the angle of θ_{nf}. θ_{R} is the Rayleigh angle, λ_{SAW} and λ_{l} denote the wavelengths of the two waves which are propagating on the $LiNbO_3$ substrate and in the fluid, respectively. (b) A schematic illustration of the stimulation system. A signal generator produces radio frequency (RF) pulses which are amplified by a power amplifier. The pulses drive the FSCS with the reference forward and reflected powers monitored by power meters. A matching network is used for maximising the power transmission. SAW pulses are produced on the $LiNbO_3$ substrate and interact with the hESCs. The inset shows the process of the stimulation process, starting from transferring the hESCs to the FSCS. After 12 days SAW stimulation, the cells are transferred to culture plates for further 10 days.

The hESCs are seeded in the platform with a periodic SAW simulation for twelve consecutive days, followed by ten-day culture in conventional culture plates as shown in the inset of Figure 1b. Afterwards, the cells are collected for RNA sequencing, quantitative polymerase chain reaction (qPCR) and immunofluorescence analysis. Three SAW dose groups with three FSCS devices in each group plus three control groups are applied in the present study.

2.2. Numerical simulation of acoustic pressure and streaming

The interaction between SAW and culture medium in the FSCS device can be explained via numerical and analytical models as shown in the inset of Figure 1a, which combines an edge wave from the PDMS-$LiNbO_3$-fluid contact point [34] and a plane wave emanated from the vibration of the $LiNbO_3$ substrate to the fluid at a Rayleigh angle θ_{R}, given by

$$\theta_{\mathrm{R}} = \sin^{-1}(C_{\mathrm{l}}/C_{\mathrm{s}}), \tag{1}$$

where C_{l} and C_{s} are the speed of sound in the fluid and the Rayleigh wave velocity in the substrate, respectively. In Figure 1a, λ_{SAW} and λ_{l} denote the wavelengths of the two waves which are propagating on the $LiNbO_3$ substrate and in the fluid, respectively. The normal component of the substrate velocity $\boldsymbol{v}$ is set as the boundary condition for acoustic coupling into the fluid. For a travelling SAW, this boundary condition [35] is determined by

$$\boldsymbol{v} = -\omega u_0 e^{-\alpha x} e^{-ikx}\,, \tag{2}$$

where ω, u_0, k, α, and x denote angular frequency, vibration amplitude, wave number, attenuation coefficient, and x coordinate, respectively. The attenuation coefficient is calculated by [35]

$$\alpha = \frac{\rho_{\mathrm{l}} C_{\mathrm{l}}}{\rho_{\mathrm{s}} C_{\mathrm{s}} \lambda_{\mathrm{SAW}}}\,, \tag{3}$$

where ρ_{l} and ρ_{s} are the densities of liquid (water, 997 kg/m^3) and substrate ($LiNbO_3$, 4,700 kg/m^3), respectively.

The plane and edge waves create interference and pressure patterns despite their continuous propagation in the fluid, which result in time-averaged pressure maxima and minima regions. A near-field pattern of acoustic pressure is formed at the $LiNbO_3$-fluid interface with the initial period given by [34]

$$P_{\mathrm{nf}} = \lambda_{\mathrm{l}}/(1 - C_{\mathrm{l}}/C_{\mathrm{s}})\,. \tag{4}$$

The angle at which the maximum and minimum fluid displacement locations project into the fluid from the $LiNbO_3$-fluid interface is given by

$$\theta_{\mathrm{nf}} = \frac{1}{2}\cos^{-1}(C_l/C_s)\,. \quad (5)$$

An impedance boundary condition was set at the PDMS-fluid interface. A region on the x-z plane with the dimensions of 1,000 μm (width, $5 \times \lambda_{\mathrm{SAW}}$) × 200 μm (height, $1 \times \lambda_{\mathrm{SAW}}$) starting from the PDMS-$LiNbO_3$-fluid contact point was numerically studied using the COMSOL Multiphysics.

2.3. Device fabrication

The FPCB design file containing the pattern of finger electrodes was submitted to a PCB prototype manufacturer (circuitfly.com) for fabrication. The FPCB contains 40 pairs of finger electrodes with a period of 200 μm and an aperture size of 2 cm. A standard PCB gold plating process was used during the development, i.e., the finger electrodes were made of bilayers of nickel/gold (2 μm/30 nm in thickness) and patterned onto a 70-μm thick polyester laminate. A coaxial cable was soldered to the busbars of the FPCB.

The assembly process of the FSCS device was started from placing the $LiNbO_3$ substrate bonded with the PDMS chamber into the slot on a 3D-printed holder (Figure. S1). Then the FPCB, the silicone pad and the rectangular nut were subsequently stacked onto the substrate. The two screws were used to fasten the stacking structure inside the holder and allow a uniform clamping force on the FPCB and the $LiNbO_3$ substrate. The silicone pad and the rectangular nut were slightly larger than the IDE region of the FPCB.

The FPCB, the PDMS chamber and the 3D-printed holder were customised and manufactured for the study, and other components were all off-the-shelf items. The specifications of all the components are given in Table S1 in the supplementary information (SI). Using the FPCB technique to fabricate the FSCS is an extraordinary time-saving strategy and eliminates the researcher's effort to access cleanroom facilities to prepare multiple SAW devices. This is very helpful for this study as any short-circuit damage caused by cell medium spillage or accidental breakdown for any of the FSCS device can be efficiently recovered and the work can carry on for the consecutive simulations over a 12-day period. One can easily replace a new $LiNbO_3$ wafer and / or a new FPCB to construct an on-demand FSCS in minutes without accessing to cleanroom for photolithography process [30, 32, 36].

Twelve-well culture plates (with its bottom area of 4 cm^2 per well) [37] and six-well culture plates (with its bottom area of 9.6 cm^2 per well) [38] are often used for growing hESCs. In this study, the PDMS chamber was designed to approximate the bottom area of the single well of the twelve-well culture plate, which has an internal dimension of 2cm (L) × 2cm (W) × 1.5cm (H). The thickness of the PDMS chamber wall was 2 mm. The PDMS chamber was formed by pouring a mixture of PDMS base and a curing agent (w/w =10:1) into a 3D-printed mould and left cured at 45ºC for overnight. A thin layer of PDMS liquid was applied to attach the PDMS chamber to the pre-cut $LiNbO_3$ substrate, and then cured at 65 ºC for 2 hours. A cover slide was loosely placed on the top of the PDMS chamber after the hESCs were seeded.

The SAW stimulation system includes RF instrument is shown in Figure 1b. The driving circuitry was consisted of a RF signal source, a power amplifier, a power meter, and a matching network. RF functional generator was used to drive the FSCS to produce SAW pulses in the cell chamber to stimulate the cells.

2.4. Device characterization

The reflection coefficient S_{11} of the FSCS was measured using a vector network analyzer (VNA, E5061B, Keysight, US). The monitoring of S_{11} is essential as it guides the design process of impedance matching. The dip frequency in S_{11} was registered as the Rayleigh mode frequency of the FSCS device to be used for the cell stimulations. The SAW amplitude was decayed along the propagation on the $LiNbO_3$ substrate due to the attenuation caused by the PDMS material and the medium inside the PDMS chamber. To determine the attenuation caused by the PDMS chamber and the medium, two further measurements were performed as detailed in the SI (Figure S2 and Figure S3). A droplet transportation experiment was performed to validate that the SAWs were effectively produced by the FPCB device, and the SAW amplitude was fully controllable. A hydrophobic layer of CYTOP™ (~200 nm, Asahi Glass Co. LTD, Japan) was coated onto the surface of the $LiNbO_3$ substrate outside the IDT region. A 1-μl sessile droplet of deionized water was placed on the hydrophobically treated area along SAW propagation pathway. A camera was used to record videos of the droplet pumping. The pumping velocity was analyzed using a video analysis package (Tracker, OSP). To measure the temperature variation of the fluid in the PDMS chamber under different SAW doses, a thermocouple was attached to the bottom of the water filled PDMS chamber. For each SAW dose, the temperature readings were taken in every two minutes.

2.5. SAW doses for hESC stimulation

Three SAW doses produced by RF amplitudes of 24V, 31V and 39V (peak-to-peak voltage) were applied to administrate stimulations of the hESCs [12, 13]. The RF signals were set to a pulse mode with a burst period of 1 ms, 200 pulses per burst, and 40% duty cycle. The pulse frequency was set to be the Rayleigh mode frequency of individual FSCS devices. A total of twelve FSCS devices were efficiently prepared owing to the rapid prototyping capability of the FPCB technique. Three FSCS devices were applied in each SAW dose group, and another three FSCS devices were applied as the control group. The three dose groups were stimulated by the SAWs for 10 min at the same time on each day, and for 12 consecutive days. The SAW stimulation was performed after replacing the differentiation medium at room temperature in the fume hood. For the three FSCS devices in the control group, the hESCs were cultured using the same differentiation medium [39] as that used in the stimulation groups and stayed at room temperature for 10 min without applying any SAW stimulation.

2.6. On-FSCS hESC culture

All the FSCS devices were sterilized by exposing them to ultraviolet radiation for overnight. Before cell seeding, vitronectin recombinant human protein (A14700, Thermo Fisher Scientific, USA) was applied to coat the FSCS device. The hESC line (H9; passage 38-44) was seeded into the PDMS chamber at a concentration of 2.5×10^5 cells/cm^2 and cultured in the monolayer culture in an incubator (37ºC, 5% CO_2) for the entire stimulation course and follow-up culture. On Day 1, all the samples were cultured with Essential 8™ Medium (A1517001, Thermo Fisher Scientific, USA) without SAW stimulation. From Day 2 to Day 13, the culture medium was replaced on a daily basis in all groups using the neural induction protocol reported in Reference [39], followed by SAW doses administrated to the stimulation groups for 10 min. On Day 13, the cells in the FSCS device were transferred to culture plates and continued to differentiate for another 10 days using the same neural induction medium without any SAW stimulation. On Day 23, the cells were collected for RNA sequencing, qPCR and immunofluorescence staining.

2.7. Whole Transcriptome Sequencing (RNA Sequencing) and Gene Ontology Enrichment Analysis

Total RNA extraction was performed using RNeasy Serum/Plasma Kit (Qiagen, USA) following the manufacturer's protocol. After the total RNA was extracted, the RNA concentration and purity were measured using the NanoDrop spectrophotometer (Thermo Fisher, USA) according to 260/280 absorbance ratio and Labchip GX Touch HT Nucleic Acid Analyzer (PerkinElmer, USA). High-quality RNA was applied for cDNA libraries construction and sequencing. The mRNA was enriched by oligo (dT) beads and the RNA sequencing libraries were generated using the KAPA Stranded RNA-Seq Kit for Illumina with multiplexing primers, according to the manufacturer's protocol. The RNA sequencing was performed using the Illumina Nova sequencer. The detailed gene ontology enrichment analysis and KEGG enrichment pathway analysis of the differentially expressed genes was included in the SI (Table S2-S7).

2.8. Quantitative PCR (qPCR) and Immunofluorescence staining

The cells from each SAW dose group were extracted for their total RNA using RNeasy Mini Kit (Qiagen, Germany). The expressions of four NSC markers, including PAX6, SOX1, NKX2-1 and SOX10, and four differential expressed genes identified in RNA Sequencing, including ALK, CENPF, PCDH17 and ACTN3 were also examined. The qPCR primer sequences are listed in Table 1. Immunocytochemistry was performed to identify development stage of the cultured cells, using antibodies against TUJ1 (MAB1637, Merck, Germany), a more mature neuron marker, and SOX2 (14-9811-80, Thermo Fisher Scientific, USA), an NSC marker. In addition, 4',6-diamidino-2-phenylindole (DAPI) was used to stain the cell nuclei. To quantify the fluorescence intensity of immunostaining, the normalised fluorescence of *Tuj1* and *Sox2* in each SAW group was calculated using ImageJ.

Table 1. The qPCR primer sequences of the four markers

Gene	**Primer (5' to 3')**	
	Forward	**Reverse**
Pax6	TCTTTGCTTGGGAAATCCG	CTGCCCGTTCAACATCCTTAG
Sox1	GGCTGAGCACCACTACGACTTAG	GAGCCAAGACCTAGATGCCAACAA
NKX2-1	AACCAAGCGCATCCAATCTCAAGG	TGTGCCCAGAGTGAAGTTTGGTCT
Sox10	CCACCTATGCCACAGTGCCTAAG	GTGCCAACTCCTTCCTGCCTTC
Alk	GTGCTCTGCTTCAATGTAGTCA	CCACATCAACAAGGCAAGGA
Cenpf	AGGAGGCAGATGAATACTTGGATA	TGGAACAACTGGACCTAGCA
Pcdh17	AGCATTCATCAGAGCACTAATTCG	GTTGTCCTTGTTCACCAATCACT
Actn3	TCGTGCGTGACATTAAGGAG	TTGCCAATGGTGATGACCTG

2.9. Statistical Analysis

Kruskal-Wallis one-way analysis of variance was performed to compare the differences of the cell densities and qPCR results among different groups. $P<0.05$ is considered as statistically significant. Fisher's least significant difference test was applied to find all pairwise differences. SPSS statistics (Version22, IBM, US) was applied to perform the statistical analysis.

3. RESULTS AND DISCUSSION

Conventional ultrasound using various waveforms, frequencies, amplitudes and transmitting patterns has been applied for neural differentiation [40, 41]. The FSCS device proposed in this study works with a much higher frequency of SAWs (~20 MHz), demonstrating the advantages of generating mechanical vibrations on the substrate where the amplitude and pattern of the vibration can be fully controlled in precision.

3.1. Characterization of the FSCS device

All the FSCS devices prepared by using the FPCB technique yielded a small inter-device variability in terms of Rayleigh mode frequency, i.e., 19.69±0.12 MHz (mean ± standard deviation). All the devices expressed a similar spectral pattern of reflection coefficient, S_{11}, with an example shown in Figure S4. The S_{11} was optimized with the use of a matching network to -41.45±6.92 dB, which indicated that the FSCS devices achieved the same level of frequency response as those SAW devices made through conventional photolithography technique in cleanroom. Power meters were used to monitor the forward and reflection powers for each FSCS device under different input powers. It was noted that the reflection power was accounted for less than ~8.6% of the forward power under all input powers, indicating efficient power delivery on the FSCS devices was achieved.

Droplet transportation tests proved that the SAW generation on the FSCS device was successfully generated, and the SAW amplitude was fully controllable through adjusting the level of the RF input signal. Figure 2a shows that the pumping velocity of the droplet, which is associated with the SAW amplitude, increases with the amplitude of RF input signals. A maximum pumping velocity of 148.91±16.63 mm/s was achieved with a continuous RF input signal of 39.2 V (peak to peak voltage). RF signals were continuously applied for the droplet transportation tests in order to produce sufficient kinetics on the droplets. It is anticipated that the SAW intensity for hESCs stimulation was much smaller using a pulse mode, whose amplitude was also fully controllable.

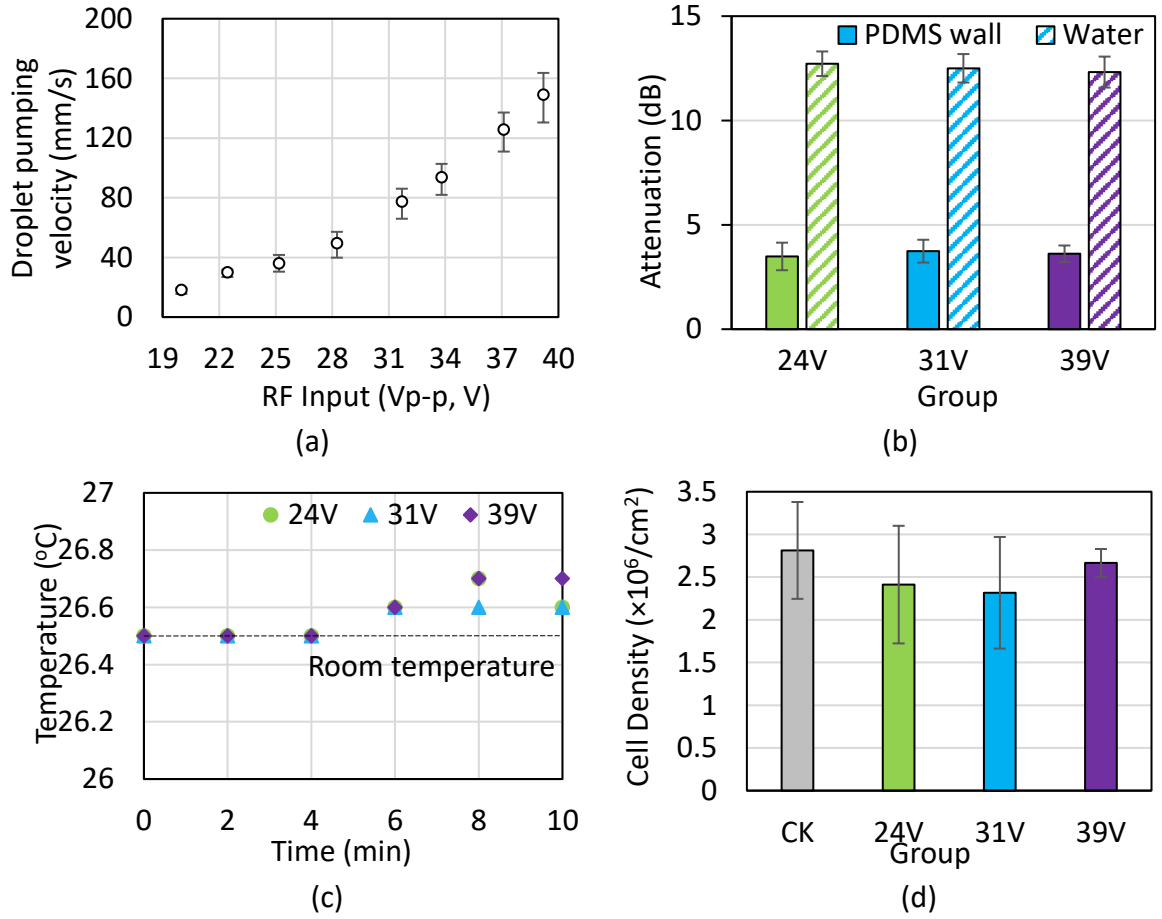

Figure 2. (a) The droplet pumping velocity on the FSCS device for three different input powers under a continuous mode. (b) Attenuations of the PDMS wall on the FSCS device and the water inside the PDMS chamber under three doses (horizontal axis is the input RF amplitude under pulse mode). (c) The PDMS chamber temperature over a 10-min course under three input

amplitudes on pulse mode. (d) The cell density of the control (CK) and three simulation groups measured after 12-day SAW stimulation.

Attenuation of the PDMS wall on SAW signals was found to be 3.61±0.52 dB at 19.69 MHz as shown in Figure 2b, i.e., ~56% of the SAW power was absorbed when encountering with the PDMS wall before reaching the hESCs. The rest of the SAWs were delivered into the cell medium inside the PDMS chamber for exerting acoustic radiation force and inducing medium streaming and also produced mechanical stimulation to the hESCs. The SAW attenuation in the medium inside the PDMS chamber is shown in Figure 2b, indicating that more than 90% of the SAW energy was converted in the cell medium into leaky SAW and heat.

The PDMS chamber filled with water shows minor rise of temperature under three input power levels of the pulse mode as shown in Figure 2c. The increase of the temperature in the stimulation chamber is less than 0.2 ºC over 10 min. Such minor temperature change is unlikely to incur notable thermal impact on the stem cells [42]. Our results of cell densities for both the control and stimulation groups after twelve consecutive days (Figure 2d (P>0.05)) confirm the biosafety of the three SAW doses which were applied.

Using FPCBs effectively saves the device's footprint (Figure S1b) and improves the flexibility to meet the requirement of hESC differentiation in the incubator. A single FPCB laminate produced all the finger electrodes for fabricating twelve FSCS devices. Thin film FPCBs were soft and flexible, which require minimum effort to form a good contact with the $LiNbO_3$ substrates to produce SAWs. This results in a good stability in reflection coefficients S_{11}. Each FSCS device interfaced with a matching network to reduce the impedance mismatching between the FSCS device and the output stage of the RF power amplifier. The S_{11} peak of the twelve FSCS devices at Rayleigh mode frequency was reduced from -7.72±2.53 dB (mean ± SD) to -41.45±6.92 dB with the matching network. Batch FSCS devices were proved to be efficiently prepared with considerable stability and reliability without a need to access cleanroom facilities. This provides a low requirement in deploying small- to pilot-scale regulation and acceleration of the hESCs using ultrasound.

3.2. Numerical simulation

Numerical analysis revealed the acoustic pressure distribution and the streaming velocity field inside the PDMS chamber. The velocity of SAW on the $LiNbO_3$ substrate along the x axis is plotted in Figure 3a, which denotes a decayed propagation leading to a first-order acoustic pressure field, $|\boldsymbol{P}_1|$, inside the PDMS chamber (Figure 3b). The acoustic pressure field has a spatial distribution consisting of decaying minimal and maximum locations arising from the PDMS-$LiNbO_3$-fluid contact point. The decrease of the acoustic pressure is due to the SAW absorption in the fluid. The projection angle of the near-field fluid displacement is found to be 33.98°. The initial period of the minimal and maximum locations in the near-field pattern of acoustic pressure is also in a good agreement with the theoretical value.

The fluid streaming induced by SAWs, which would have significant impact on cells [23], is displayed by a time-averaged second-order velocity field $\langle \boldsymbol{v}_2 \rangle$ as shown in Figure 3c. The white arrows indicate the direction and magnitude of the streaming circulation velocities. Streaming vortices are observed on the x-z plane next to the $LiNbO_3$-fluid interface. The induced micro-circulations close to the surface of the $LiNbO_3$ is also a key factor for stimulating the hESCs. In addition, direct contact between the hESCs and the vibrational $LiNbO_3$ surface, together with the acoustic pressure and the fluid streaming established in the FSCS device are the

mechanical stimuli to modulate the cellular behaviours, resulting in biological effects such as activation of shear stress sensors and perforation of the cell membrane [23, 43].

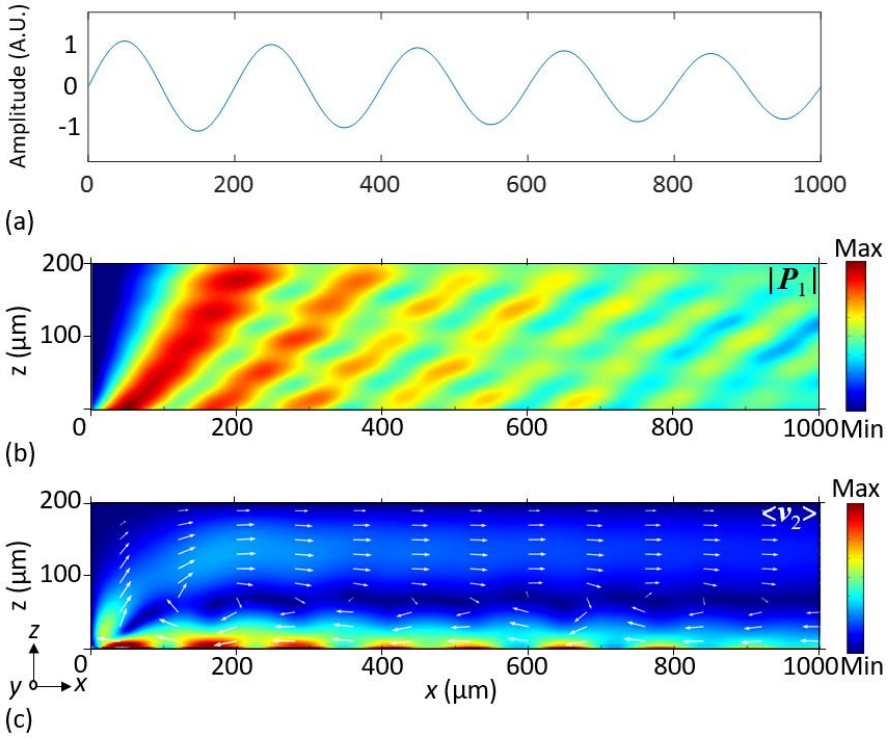

Figure 3. Numerical simulation of the acoustofluidic field on the x-z plane. (a) The velocity boundary condition applied to $LiNbO_3$ substrate. (b) The first-order pressure $|\boldsymbol{P}_1|$ for the cross section of the PDMS chamber. (c) Time-averaged second-order velocity field $\langle \boldsymbol{v}_2 \rangle$ for the cross section of the PDMS chamber.

3.3. SAW-mediated neural differentiation

The physical effects of Rayleigh SAWs are complex, including vibration of the piezoelectric substrate, and the acoustic pressure (Figure 3b) and acoustic streaming (Figure 3c) induced by the leaky SAW into the liquid as shown in the numerical simulations. In our study, the hESCs are attached onto the vitronectin-coated $LiNbO_3$ substrate, whose surface vibration creates a steady inner boundary streaming generating Rayleigh streaming vortices [44]. The surface vibration on the $LiNbO_3$ substrate together with the induced streaming trigger the stem cells' responses thus resulting in the acceleration of differentiation [45]. The combination of plane and edge waves (shown in Figure. 1a) with locally oscillatory shear flows around the cells resulting in the activation of mechano-sensitive ion channels on the stem cells [46]. Electromagnetic radiation generated by the RF signal in the SAW devices has shown minor effect on biological samples as reported in reference [22]. The thermal effect is neglectable as the temperature rise caused by the pulsed SAWs is minimal (less than 0.2 °C as shown in Figure. 2c).

Results of Differentially Expressed Genes (DEGs) induced by SAW stimulation were identified by RNA sequencing as shown in Figure 4. DESeq2 [47] was performed to select DEGs between each experimental and the control group. As shown in Figure 4, a total of 487 DEGs are identified in the three experimental groups. The *P* value of 0.05 and a fold change of 2 were selected as the cutoff values. Among the DEGs of the three experimental groups, three up-regulation genes of *ALK*, *CENPF, PCDH17* and one down-regulation gene of *ACTN3* are noted. The *ALK* is related to the neural development [48]. *CENPF* is involved with the cell cycle-transport events [49]. *PCDH17* participates in specific cell-cell connections, which is also one

of the DEGs found in the induced pluripotent stem cell derived neural crest stem cell induced by LIPUS [50]. *ACTN3* is involved in remodeling of adherent junctions and is critical for neural regeneration [51].

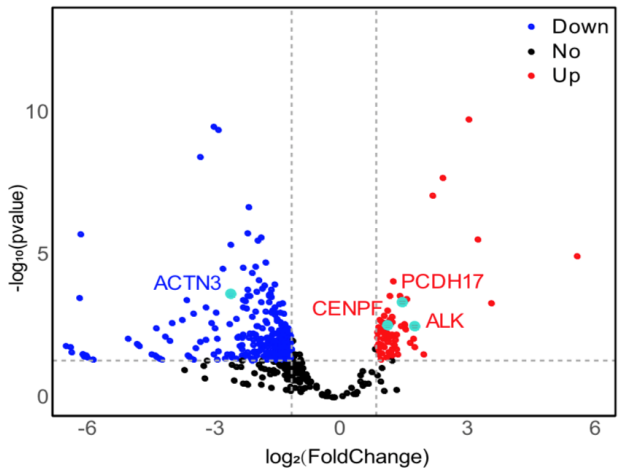

(a)

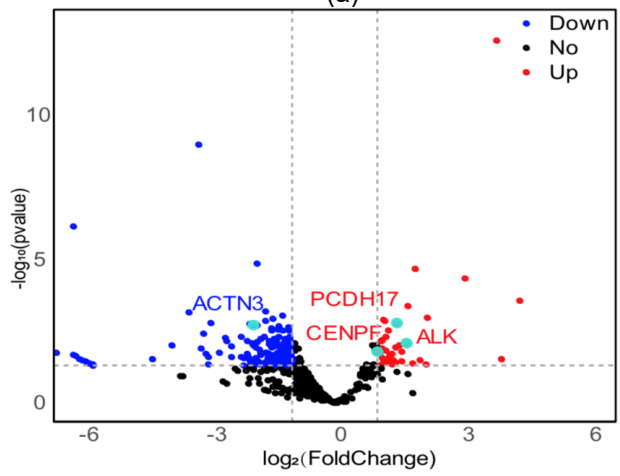

(b)

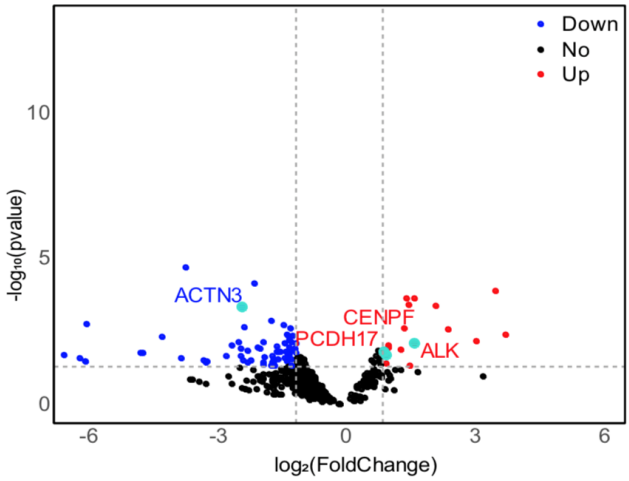

(c)

Figure 4. The differential expressed genes between (a) 24V, (b) 31V, (c) 39V FSCS experimental groups and the control group

Gene ontology analysis (Figure 5) of all significantly varied genes revealed the possible underpinning mechanism of the cell responses to the SAW stimulations. In comparison to the

control group, variations in the cell-cell adhesion (cell-cell junction, ECM, integrin binding) gene expression were found in all three dose groups. The gene expression patterns are associated with the SAW doses, implying that the neural differentiation process is regulated by the applied stimuli. More cell development related gene categories are changed in the 24V dose group (Figure 5a), while more cell cycle (nuclear division, positive regulation of cell cycle) and cytoskeleton (actin filament, actin binding, and actin monomer binding) related gene categories are found in the 39V dose group (Figure 5c). In addition, both cell development and cycle gene categories are existed in the 31V dose group (Figure 5b).

These results confirm the multiple effects of SAW stimulation in the gene expression levels, and more importantly, various SAW doses lead to different cell development status. The cells stimulated under low SAW doses exhibit enhanced development/differentiation-related gene expressions, which indicates that the neural differentiation process has been accelerated by the SAWs. On the other hand, more cell cycle and cytoskeleton-related genes are enriched in the high SAW dose stimulated cells. After the neural maturation, the later stage of neural development requires the cell cycle exit, neural migration and cytoskeleton rearrangement [52-54]. The results shown in Figure 5 suggest that the high SAW dose stimulated cells have entered a more mature status compared to those of low dose stimulated cells. More KEGG enrichment pathway analysis can been seen in Figure S5.

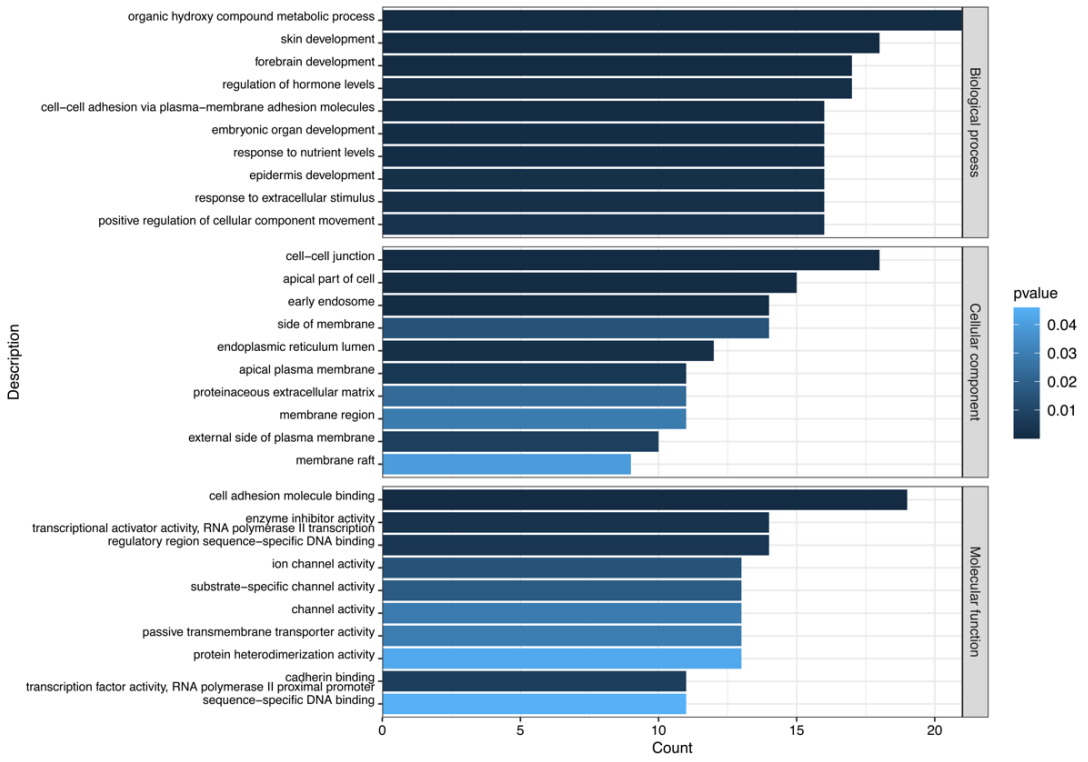

(a)

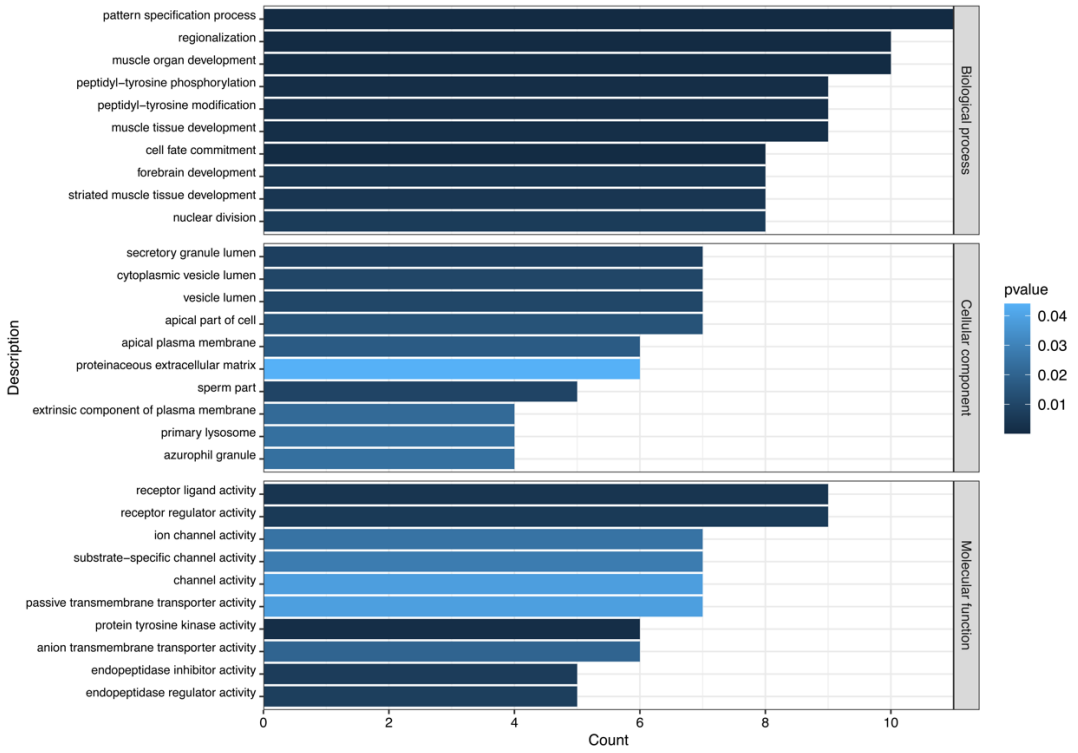

(b)

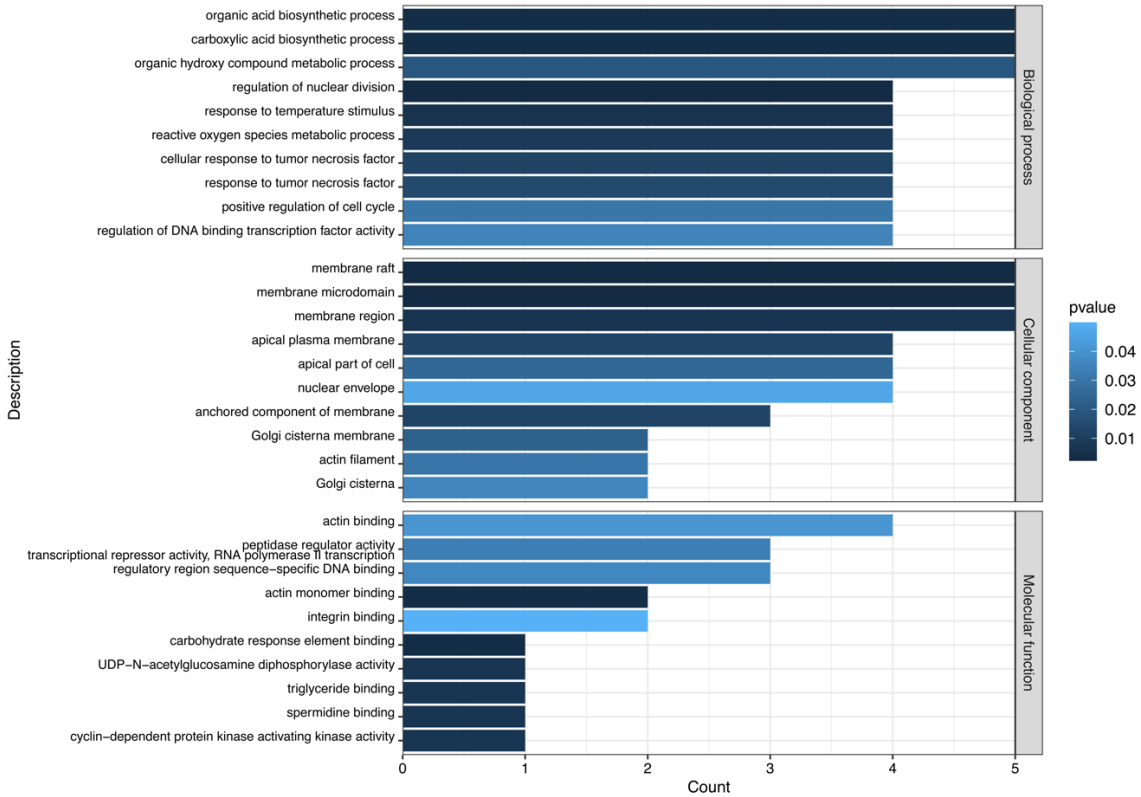

(c)

Figure 5. Gene ontology analysis of all the significantly varied genes in different SAW dose groups v.s. control group (top ten items in each biological concept). (a) 24V-, (b) 31V-, (c) 39V-SAW-treated versus Control hESCs. The number of genes in each category is shown on the *x*-axis as count value (see also Supplementary Data, Table S2-S4)

In order to validate the results of RNA sequencing, the relative expression of NSC marker genes, *Pax6, Sox1*, *Sox10* and *Nkx2-1*, was examined by the qPCR, and the results are shown in Figure 6. The expression of these NSC marker genes was decreased in at least one SAW dose group compared with the control group except *Nkx2-1*. Interestingly, it was demonstrated that the relative expression of *Sox1* gene showed a decreasing trend which was negatively correlated with the SAW power. Since these NSC markers were highly expressed in the early stage of neurogenesis and gradually decreased in relatively mature neurons, these results suggested that the neural differentiation process was accelerated by SAW stimulations and thus the neural differentiation potential of stem cells was enhanced. Notably, the expression of *Pax6* and *Sox10* was decreased significantly in the low or medium SAW dose groups, but not in the high SAW dose group (Figures 6a & 6c). To further confirm the different gene expression profile by various SAW doses, the three up-regulated genes, *Alk*, *Cenpf*, and *Pcdh17*, as well as one down-regulated gene, *Actn3*, were also examined by qPCR as shown in Figures 6e-6h. Significant variations in these four DEGs were noted in all SAW dose groups, which are similar to the findings in RNA sequencing. These observations reinforce that for the RNA sequencing, more stem cell development/differentiation-related genes were altered in the low and medium SAW dose groups, but not in the high SAW dose group.

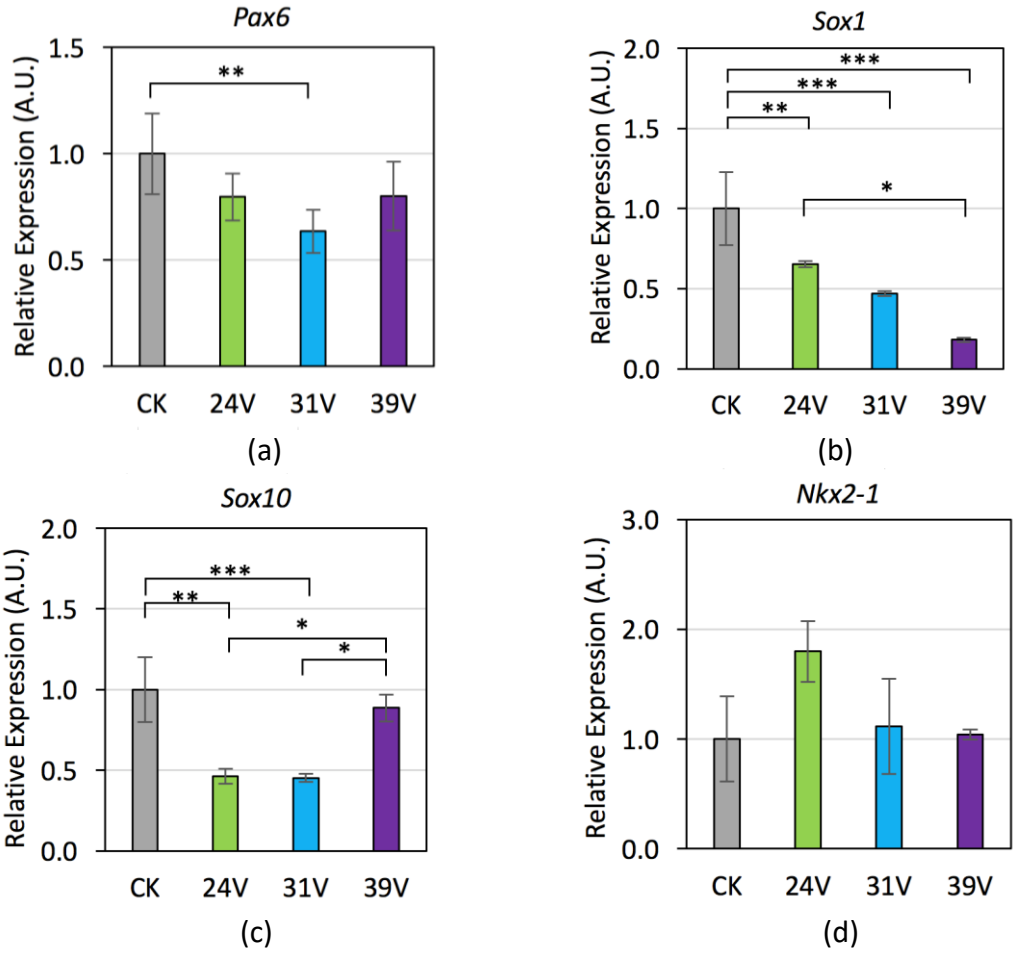

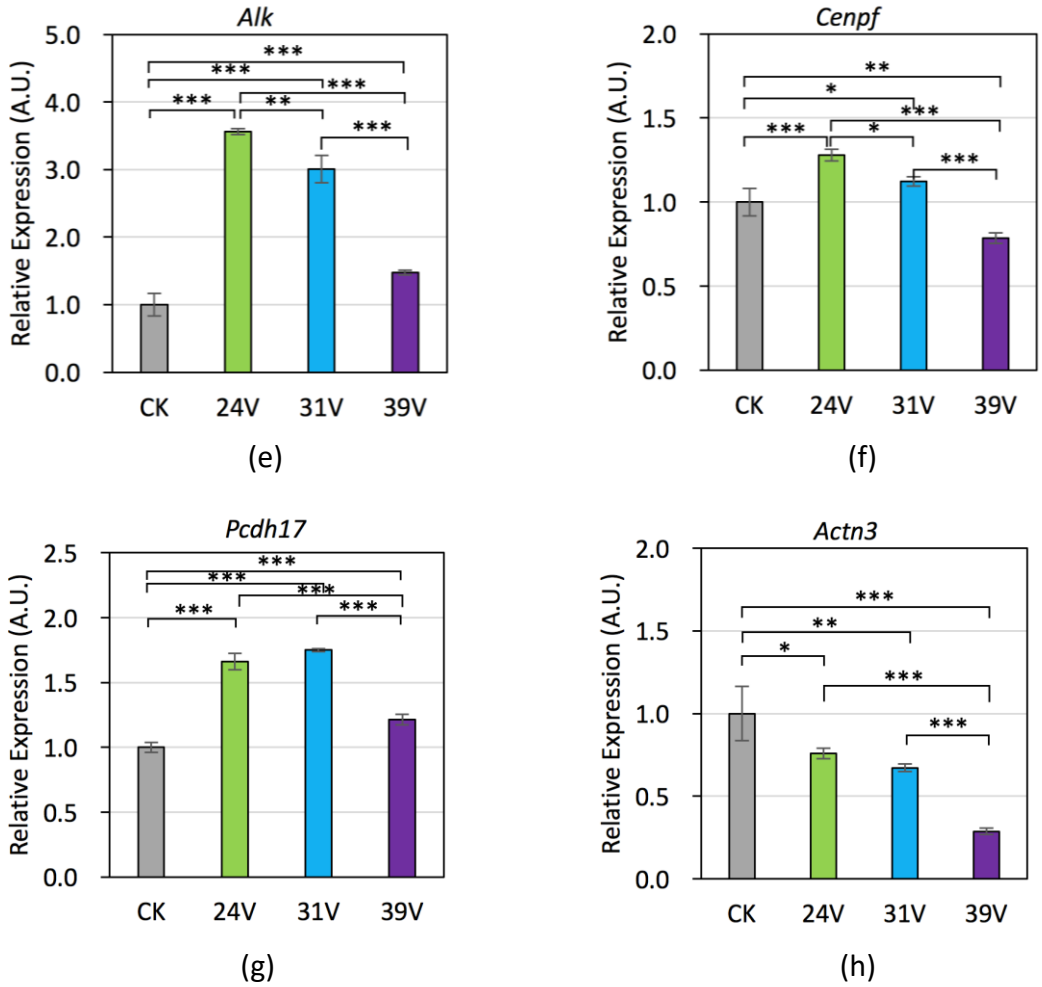

Figure 6. The qPCR results for the expression of neural stem cell maker genes (a) *Pax6*, (b) *Sox1*, (c) *Sox10*, (d) *Nkx2-1*, (e) *Alk*, (f) *Cenpf*, (g) *Pcdh17*, and (h) *Actn3* immediately after 12-day stimulation in the FSCS devices under three different SAW doses (*: $P<0.05$, **: $P<0.01$, ***: $P<0.005$).

Since the high SAW dose led to the change of more cell cycle, ECM, and cytoskeleton-related genes, further investigation was carried out to clarify the development status of the cells stimulated by different SAW doses. Formation of neural rosettes from the NSCs is an essential morphogenetic process during the early neural development, which requires the cytoskeletal rearrangements triggered by extracellular cues [55]. The 31V and 39V SAW dose groups resulted in a more discrete cell morphologic pattern, which assembles the mature neuron phenotype (white arrows in Figures 7c & 7d). Whereas the 24V dose group exhibited a phenotypic feature that is commonly noted as the neural rosettes as developed in the control group (yellow arrows in Figures 7a & 7b). These results indicated that the high SAW doses may help shorten the neural differentiation process and the cells treated with high SAW dose exhibited a more mature neuron-like morphology. Regulation and acceleration to the neural lineage differentiation process of stem cells is achieved by applying appropriate SAW dosage.

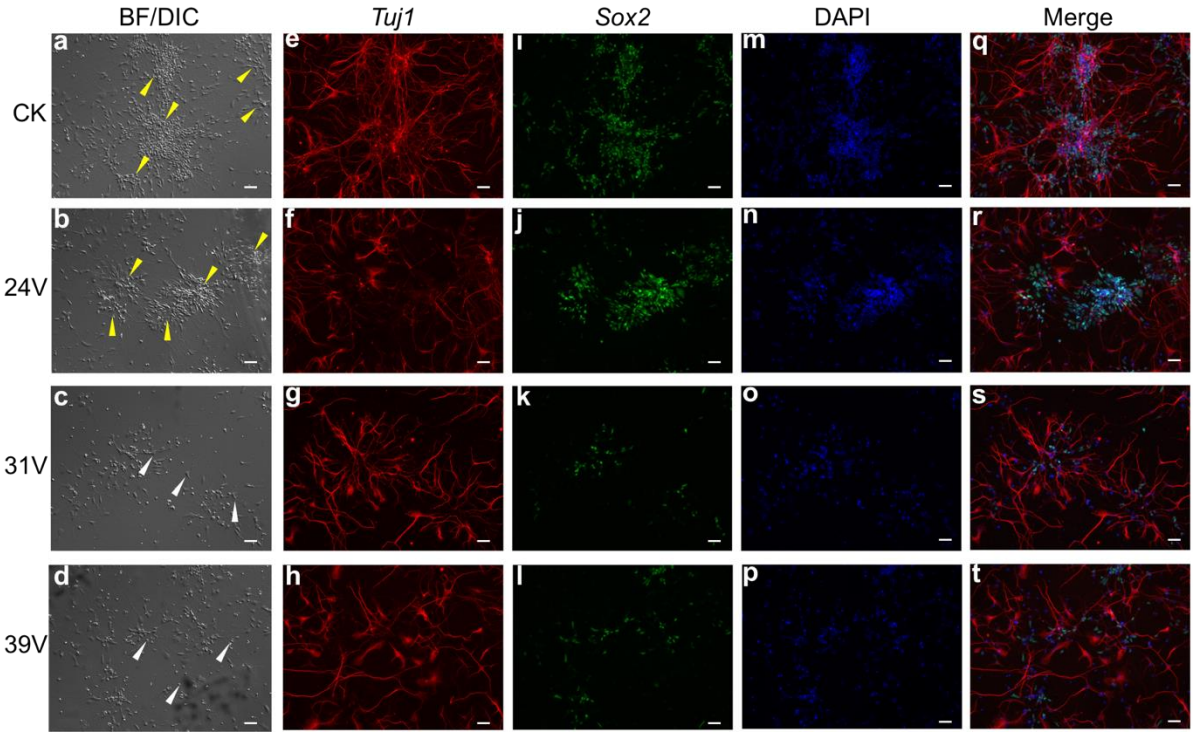

Figure 7. The immunofluorescence of neural differentiation of hESCs 10 days after the SAW stimulation with three different doses. (a-d) Differential interference contrast (DIC) images, in which yellow arrows indicate phenotypic features analogous to neural rosettes and white arrows point out representative discrete stem cells. Immunofluorescence images for (e-h) *Tuj1* (red), (i-l) *Sox2* (green), (m-p) DAPI (blue) and (q-t) merged staining. Scale bar: 50 μm.

Moreover, the matureness of the SAW stimulated cells was assessed by immunostaining using the more mature post-mitotic neuron marker *Tuj1* (red stain in Figures. 7e-7h) and antibodies against the neural progenitor lineage marker *Sox2* (green stain in Figures. 7i-7l). Although less cells are presented in the 31V and 39V dose groups as revealed by the DAPI staining (blue stain in Figures. 7m-7p), the *Tuj1*+ cell population in these two groups is comparable to that in the control and 24V groups (Figures. 7e-h). The percentage of cells expressing *Tuj1*+ marker was calculated based on the normalised fluorescence intensity of *Tuj1*/DAPI to the corresponding control group (Figure. 8a). The results show that the ratios of *Tuj1*+ mature neuron-like cells in 31V and 39V are higher than those of the control and 24V groups. Conversely, the ratios of the *Sox2*+ cells in the 31V and 39V dose groups are significantly less than those in the control and 24V dose groups (Figures. 7i-7l and Figure. 8b). These results further consolidate that the cells in the high SAW dose group were differentiated into more mature neural lineage than those in the control and the low dose groups. The mature neural cell types, such as glial cells and mature neurons, were not presented in the current form of progenitor cells. This was proved by the flow cytometry analysis as shown in Figure S6, in which the differentiated cell population is homogeneous as identified by PAX6 of ~98.97%, a marker of neural stem cells or progenitor cells.

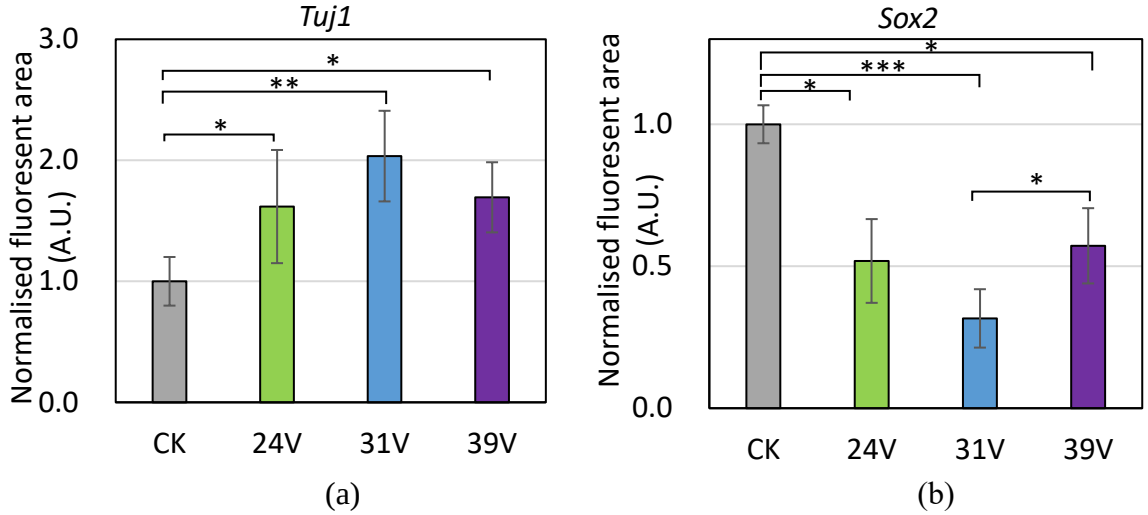

(a) (b)

Figure 8. The normalized fluorescent area of (a) Tuj1 / DAPI and (b) Sox2 / DAPI of all SAW dose groups and the control group (*: P<0.05, **: P<0.01, ***: P<0.005).

Transcriptome analysis deciphers more genes involved in the development of forebrain, skin, epidermis, muscle organ, etc., altered in the low SAW dose groups of 24V and 31V. However, more cellular components, such as membrane raft, microdomain, actin filament, and related genes are regulated in the high SAW dose group of 39V, indicating that SAW dosage can be used to regulate cellular responses. Both ECM (cell-cell junction, adhesion, actin filament, and integrin binding) and cellular signaling pathway (ion channel activity, receptor ligand, and transmembrane transporter activity) related genes were altered in all three groups. As the mechano-transduction sensitive elements, regulating ECM and cell-cell junction allows to transmit the forces, modulate the maturation or disassemble these adhesions, and initiate intracellular signaling cascades that ultimately altered the cellular behaviors [56, 57]. Additionally, the modulation of ion channel activity and raft on the cell membrane [58] led to the enhanced downstream signaling pathways which accelerated the cell development process [59]. Moreover, the integrin-ECM interaction and actin cytoskeleton were shown to mediate neuronal development and function, suggesting a possible mechanism of SAW mediated neuronal development acceleration via regulation of ECM and cytoskeleton [60, 61].

4. CONCLUSIONS

This study presented the FSCS devices deploying in SAW mediation of neural differentiation process of the hESCs. This study demonstrated the capability of the SAW device in acceleration of maturation of neurons derived from the hESCs. The FSCS devices were fabricated through a fast-prototyping process by clamping the FPCB to the piezoelectric substrate, which enabled rapid manufacturing of acoustofluidic devices for batch deployment in biomedical applications. The way of SAW production in the FSCS device allowed concentrating acoustic energy on the propagation surface, which applied direct mechanical perturbations on the hESCs. SAW also induced acoustic pressure and streaming in the hESC medium exhibiting shear stress on the hESCs. Further analysis on the SAW-stimulated neural cells, including RNA sequencing, qPCR and immunofluorescence staining, indicated that low SAW dose led to more changes in neural development/differentiation-related gene expression, while high SAW dose mainly altered the cell cycle, ECM, and cytoskeleton-related gene expression. The hESCs stimulated by high SAW dosage presented a relatively more mature neuron status than the control group. Altogether, the FSCS device offered a robust SAW stimulation tool for acceleration of hESC differentiation towards more mature neural lineage, which may benefit and promote the

application of stem cell-derived neural cell therapy in disease modeling, drug screening, and regenerative medicine.

ACKNOWLEDGEMENTS

This work was supported by the Natural Science Basic Research Program of Shaanxi Province [grant number 2020JQ-233]; the Engineering and Physical Sciences Research Council (EPSRC) [grant numbers EP/P002803/1 and EP/P018998/1]; Special Interest Group for Acoustofluidics from UK Fluids Network (EP/N032861/1), and the International Exchange Grants from Royal Society [grant numbers IEC/NSFC/170142, IEC/NSFC/201078], and EPSRC NetworkPlus in Digitalised Surface Manufacturing (EP/S036180/1).

Reference

[1] O. Lindvall, Z. Kokaia, Stem cells for the treatment of neurological disorders, Nature 441(7097) (2006) 1094-1096.

[2] S. Corti, M. Nizzardo, M. Nardini, C. Donadoni, S. Salani, D. Ronchi, C. Simone, M. Falcone, D. Papadimitriou, F. Locatelli, N. Mezzina, F. Gianni, N. Bresolin, G.P. Comi, Embryonic stem cell-derived neural stem cells improve spinal muscular atrophy phenotype in mice, Brain 133(2) (2010) 465-481.

[3] R. De Gioia, F. Biella, G. Citterio, F. Rizzo, E. Abati, M. Nizzardo, N. Bresolin, G.P. Comi, S. Corti, Neural Stem Cell Transplantation for Neurodegenerative Diseases, International Journal of Molecular Sciences 21(9) (2020).

[4] M. Wang, Z. Xu, Q. Liu, W. Sun, B. Jiang, K. Yang, J. Li, Y. Gong, Q. Liu, D. Liu, X. Li, Nongenetic optical modulation of neural stem cell proliferation and neuronal/glial differentiation, Biomaterials 225 (2019) 119539.

[5] W. Guo, X. Zhang, X. Yu, S. Wang, J. Qiu, W. Tang, L. Li, H. Liu, Z.L. Wang, Self-Powered Electrical Stimulation for Enhancing Neural Differentiation of Mesenchymal Stem Cells on Graphene-Poly(3,4-ethylenedioxythiophene) Hybrid Microfibers, ACS Nano 10(5) (2016) 5086-5095.

[6] W. Zhu, T. Ye, S.J. Lee, H. Cui, S. Miao, X. Zhou, D. Shuai, L.G. Zhang, Enhanced neural stem cell functions in conductive annealed carbon nanofibrous scaffolds with electrical stimulation, Nanomedicine: Nanotechnology, Biology, and Medicine 14(7) (2018) 2485-2494.

[7] G. Liu, X.M. Li, S. Tian, R.R. Lu, Y. Chen, H.Y. Xie, K.W. Yu, J.J. Zhang, J.F. Wu, Y.L. Zhu, Y. Wu, The effect of magnetic stimulation on differentiation of human induced pluripotent stem cells into neuron, Journal of Cellular Biochemistry 121(10) (2020) 4130-4141.

[8] D. Desmaële, M. Boukallel, S. Régnier, Actuation means for the mechanical stimulation of living cells via microelectromechanical systems: A critical review, Journal of Biomechanics 44(8) (2011) 1433-1446.

[9] Y. K, J. H, L. HR, L. JS, K. SR, S. KY, C. E, B. J, I. SG, C. SW, Multiscale, hierarchically patterned topography for directing human neural stem cells into functional neurons, ACS nano 8(8) (2014) 7809-22.

[10] E.L. Moreno, S. Hachi, K. Hemmer, S.J. Trietsch, A.S. Baumuratov, T. Hankemeier, P. Vulto, J.C. Schwamborn, R.M.T. Fleming, Differentiation of neuroepithelial stem cells into functional dopaminergic neurons in 3D microfluidic cell culture, Lab on a Chip 15(11) (2015) 2419-2428.

[11] I.C. Lee, H.-J. Wu, H.-L. Liu, Dual-Frequency Ultrasound Induces Neural Stem/Progenitor Cell Differentiation and Growth Factor Utilization by Enhancing Stable Cavitation, ACS Chemical Neuroscience 10(3) (2019) 1452-1461.

[12] Y. Lv, P. Zhao, G. Chen, Y. Sha, L. Yang, Effects of low-intensity pulsed ultrasound on cell viability, proliferation and neural differentiation of induced pluripotent stem cells-derived neural crest stem cells, Biotechnol Lett 35(12) (2013) 2201-12.

[13] X. B, C. G, Z. Y, Y. L, P. J, L. Y, Low-intensity pulsed ultrasound combination with induced pluripotent stem cells-derived neural crest stem cells and growth differentiation factor 5 promotes sciatic nerve regeneration and functional recovery, Journal of tissue engineering and regenerative medicine 13(4) (2019) 625-636.
[14] M. Baudoin, J.L. Thomas, Acoustic Tweezers for Particle and Fluid Micromanipulation, Annual Review of Fluid Mechanics 52(1) (2020) 205-234.
[15] N.R. Skov, H. Bruus, Modeling of microdevices for SAW-based acoustophoresis-A study of boundary conditions, Micromachines 7(10) (2016).
[16] Y. Gao, A.K. Fajrial, T. Yang, X. Ding, Emerging on-chip surface acoustic wave technology for small biomaterials manipulation and characterization, Biomaterials Science (2021).
[17] S. Li, F. Ma, H. Bachman, C.E. Cameron, X. Zeng, T.J. Huang, Acoustofluidic bacteria separation, Journal of Micromechanics and Microengineering 27(1) (2017).
[18] C. Chen, Y. Gu, J. Philippe, P. Zhang, H. Bachman, J. Zhang, J. Mai, J. Rufo, J.F. Rawls, E.E. Davis, N. Katsanis, T.J. Huang, Acoustofluidic rotational tweezing enables high-speed contactless morphological phenotyping of zebrafish larvae, Nature Communications 12(1) (2021) 1118.
[19] J. Zhang, S. Yang, C. Chen, J.H. Hartman, P.H. Huang, L. Wang, Z. Tian, P. Zhang, D. Faulkenberry, J.N. Meyer, T.J. Huang, Surface acoustic waves enable rotational manipulation of Caenorhabditis elegans, Lab on a Chip 19(6) (2019) 984-992.
[20] M. Wu, C. Chen, Z. Wang, H. Bachman, Y. Ouyang, P.-H. Huang, Y. Sadovsky, T.J. Huang, Separating extracellular vesicles and lipoproteins via acoustofluidics, Lab on a Chip 19(7) (2019) 1174-1182.
[21] M.E.M. Stamp, M.S. Brugger, A. Wixforth, C. Westerhausen, Acoustotaxis – in vitro stimulation in a wound healing assay employing surface acoustic waves, Biomaterials Science 4(7) (2016) 1092-1099.
[22] M.S. Brugger, K. Baumgartner, S.C.F. Mauritz, S.C. Gerlach, F. Röder, C. Schlosser, R. Fluhrer, A. Wixforth, C. Westerhausen, Vibration enhanced cell growth induced by surface acoustic waves as in vitro wound-healing model, Proceedings of the National Academy of Sciences 117(50) (2020) 31603.
[23] G. Greco, M. Agostini, I. Tonazzini, D. Sallemi, S. Barone, M. Cecchini, Surface-Acoustic-Wave (SAW)-Driven Device for Dynamic Cell Cultures, Analytical Chemistry 90(12) (2018) 7450-7457.
[24] C. Devendran, J. Carthew, J.E. Frith, A. Neild, Cell Adhesion, Morphology, and Metabolism Variation via Acoustic Exposure within Microfluidic Cell Handling Systems, Advanced Science 6(24) (2019).
[25] S. Ramesan, A.R. Rezk, C. Dekiwadia, C. Cortez-Jugo, L.Y. Yeo, Acoustically-mediated intracellular delivery, Nanoscale 10(27) (2018) 13165-13178.
[26] S. Ramesan, A.R. Rezk, P.M. Cevaal, C. Cortez-Jugo, J. Symons, L.Y. Yeo, Acoustofection: High-Frequency Vibrational Membrane Permeabilization for Intracellular siRNA Delivery into Nonadherent Cells, ACS Applied Bio Materials 4(3) (2021) 2781-2789.
[27] B. Kang, S. Jo, J. Baek, F. Nakamura, W. Hwang, H. Lee, Role of mechanical flow for actin network organization, Acta Biomaterialia 90 (2019) 217-224.
[28] K.H. Vining, D.J. Mooney, Mechanical forces direct stem cell behaviour in development and regeneration, Nature Reviews Molecular Cell Biology 18(12) (2017) 728-742.
[29] D. Peng, W. Tong, D.J. Collins, M.R. Ibbotson, S. Prawer, M. Stamp, Mechanisms and Applications of Neuromodulation Using Surface Acoustic Waves-A Mini-Review, Frontiers in neuroscience 15 (2021) 629056-629056.
[30] R. Mikhaylov, F. Wu, H. Wang, A. Clayton, C. Sun, Z. Xie, D. Liang, Y. Dong, F. Yuan, D. Moschou, Z. Wu, M.H. Shen, J. Yang, Y. Fu, Z. Yang, C. Burton, R.J. Errington, M. Wiltshire,

X. Yang, Development and characterisation of acoustofluidic devices using detachable electrodes made from PCB, Lab on a Chip 20(10) (2020) 1807-1814.
[31] K.B. Lee, J.R. Kim, G.C. Park, H.K. Cho, Feasibility test of a liquid film thickness sensor on a flexible printed circuit board using a three-electrode conductance method, Sensors (Switzerland) 17(1) (2017).
[32] C. Sun, R. Mikhaylov, Y. Fu, F. Wu, H. Wang, X. Yuan, Z. Xie, D. Liang, Z. Wu, X. Yang, Flexible Printed Circuit Board as Novel Electrodes for Acoustofluidic Devices, IEEE Transactions on Electron Devices 68(1) (2021) 393-398.
[33] J. Shi, X. Mao, D. Ahmed, A. Colletti, T.J. Huang, Focusing microparticles in a microfluidic channel with standing surface acoustic waves (SSAW), Lab on a Chip 8(2) (2008) 221-223.
[34] C. Devendran, D.J. Collins, Y. Ai, A. Neild, Huygens-Fresnel Acoustic Interference and the Development of Robust Time-Averaged Patterns from Traveling Surface Acoustic Waves, Physical Review Letters 118(15) (2017).
[35] J.D.N. Cheeke, Fundamentals and Applications of Ultrasonic Waves (2nd Edition), CRC Press2017.
[36] R. Mikhaylov, M. Stringer, P. Dumcius, H. Wang, F. Wu, X. Zhang, F. Alghamdi, V. Akhimien, C. Sun, A. Clayton, Y.Q. Fu, L. Ye, Z. Dong, X. Yang, A Reconfigurable and Portable Acoustofluidic System Based on Flexible Printed Circuit Board for the Manipulation of Microspheres, Journal of Micromechanics and Microengineering 31 (2021).
[37] Y. Ren, Y. Qiang, X. Duan, Z. Li, The distinct difference in azido sugar metabolic rate between neural stem cells and fibroblasts and its application for decontamination of chemically induced neural stem cells, Chemical Communications 56(15) (2020) 2344-2347.
[38] J. Zhang, J. Zhao, Y. Chen, H. Shi, X. Huang, Y. Wang, Y. Wang, Y. Wei, W. Xue, J. Han, Effect of mGluR7 on proliferation of human embryonic neural stem cells, Medicine 98(9) (2019) e14683-e14683.
[39] S.M. Chambers, C.A. Fasano, E.P. Papapetrou, M. Tomishima, M. Sadelain, L. Studer, Highly efficient neural conversion of human ES and iPS cells by dual inhibition of SMAD signaling, Nature biotechnology 27(3) (2009) 275-280.
[40] A. Amini, S. Chien, M. Bayat, Impact of Ultrasound Therapy on Stem Cell Differentiation - A Systematic Review, Curr Stem Cell Res Ther 15(5) (2020) 462-472.
[41] M. Hoop, X.-Z. Chen, A. Ferrari, F. Mushtaq, G. Ghazaryan, T. Tervoort, D. Poulikakos, B. Nelson, S. Pané, Ultrasound-mediated piezoelectric differentiation of neuron-like PC12 cells on PVDF membranes, Scientific Reports 7(1) (2017) 4028.
[42] Y. Reissis, E. García-Gareta, M. Korda, G.W. Blunn, J. Hua, The effect of temperature on the viability of human mesenchymal stem cells, Stem cell research & therapy 4(6) (2013) 139.
[43] E. VanBavel, Effects of shear stress on endothelial cells: Possible relevance for ultrasound applications, Progress in Biophysics and Molecular Biology 93(1) (2007) 374-383.
[44] C. Chen, S.P. Zhang, Z. Mao, N. Nama, Y. Gu, P.H. Huang, Y. Jing, X. Guo, F. Costanzo, T.J. Huang, Three-dimensional numerical simulation and experimental investigation of boundary-driven streaming in surface acoustic wave microfluidics, Lab on a Chip 18(23) (2018) 3645-3654.
[45] Y. Kurashina, C. Imashiro, M. Hirano, T. Kuribara, K. Totani, K. Ohnuma, J. Friend, K. Takemura, Enzyme-free release of adhered cells from standard culture dishes using intermittent ultrasonic traveling waves, Communications Biology 2(1) (2019) 393.
[46] L.A. Ambattu, A. Gelmi, L. Yeo, Short-Duration High Frequency MegaHertz-Order Nanomechanostimulation Drives Early and Persistent Osteogenic Differentiation in Mesenchymal Stem Cells, Small (2022) 2106823.
[47] M.I. Love, W. Huber, S. Anders, Moderated estimation of fold change and dispersion for RNA-seq data with DESeq2, Genome Biology 15(12) (2014) 550.

[48] I. Janoueix-Lerosey, L. Lopez-Delisle, O. Delattre, H. Rohrer, The ALK receptor in sympathetic neuron development and neuroblastoma, Cell and Tissue Research 372(2) (2018) 325-337.
[49] K.M. Loftus, H. Cui, E. Coutavas, D.S. King, A. Ceravolo, D. Pereiras, S.R. Solmaz, Mechanism for G2 phase-specific nuclear export of the kinetochore protein CENP-F, Cell Cycle 16(15) (2017) 1414-1429.
[50] B. Xia, Y. Zou, Z. Xu, Y.J.B. Lv, a. biochemistry, Gene expression profiling analysis of the effects of low-intensity pulsed ultrasound on induced pluripotent stem cell–derived neural crest stem cells, Biotechnology and applied biochemistry 64(6) (2017) 927-937.
[51] S. Yi, X.-H. Wang, L.-Y. Xing, Transcriptome analysis of adherens junction pathway-related genes after peripheral nerve injury, Neural regeneration research 13(10) (2018) 1804.
[52] L. Penazzi, L. Bakota, R. Brandt, Chapter Three - Microtubule Dynamics in Neuronal Development, Plasticity, and Neurodegeneration, in: K.W. Jeon (Ed.), International Review of Cell and Molecular Biology, Academic Press2016, pp. 89-169.
[53] J.D. Godin, L. Nguyen, Novel Functions of Core Cell Cycle Regulators in Neuronal Migration, in: L. Nguyen, S. Hippenmeyer (Eds.), Cellular and Molecular Control of Neuronal Migration, Springer Netherlands, Dordrecht, 2014, pp. 59-74.
[54] P.K. Politis, D. Thomaidou, R. Matsas, Coordination of cell cycle exit and differentiation of neuronal progenitors, Cell cycle (Georgetown, Tex.) 7(6) (2008) 691-7.
[55] M.J. Harding, H.F. McGraw, A. Nechiporuk, The roles and regulation of multicellular rosette structures during morphogenesis, Development 141(13) (2014) 2549.
[56] F. Gattazzo, A. Urciuolo, P. Bonaldo, Extracellular matrix: a dynamic microenvironment for stem cell niche, Biochim Biophys Acta 1840(8) (2014) 2506-19.
[57] C.S. Chen, J. Tan, J. Tien, Mechanotransduction at Cell-Matrix and Cell-Cell Contacts, Annual Review of Biomedical Engineering 6(1) (2004) 275-302.
[58] B.A. Tsui-Pierchala, M. Encinas, J. Milbrandt, E.M. Johnson, Jr., Lipid rafts in neuronal signaling and function, Trends in Neurosciences 25(8) (2002) 412-417.
[59] L. Decker, W. Baron, C. French-Constant, Lipid rafts: microenvironments for integrin-growth factor interactions in neural development, Biochem Soc Trans 32(Pt3) (2004) 426-30.
[60] D.O. Clegg, K.L. Wingerd, S.T. Hikita, E.C. Tolhurst, Integrins in the development, function and dysfunction of the nervous system, Frontiers in bioscience: a journal and virtual library 8(4) (2003) d723-d750.
[61] T.R. Cheever, J.M. Ervasti, Actin isoforms in neuronal development and function, International review of cell and molecular biology 301 (2013) 157-213.